Stochastic resonance in a fundamental quantum system

1999 J. Phys. A: Math. Gen. 32 2895

(http://iopscience.iop.org/0305-4470/32/15/015)

J. Phys. A: Math. Gen. **32** (1999) 2895–2919. Printed in the UK PII: S0305-4470(99)00516-8

Stochastic resonance in a fundamental quantum system

Thomas Wellens and Andreas Buchleitner

Max-Planck-Institut für Quantenoptik, Hans-Kopfermann-Strasse 1, D-85748 Garching, Germany

Received 22 December 1998, in final form 9 February 1999

Abstract. We provide a detailed description of the response of an experimentally accessible, open, driven quantum system in its stationary state to a weak periodic signal. The system, a single mode of the quantized radiation field in coherent interaction with a sequence of two-level atoms and coupled to an environment of temperature T, is shown to exhibit stochastic resonance on output, under changes of T. Furthermore, at vanishing temperature, the transition rates between the metastable states of the radiation field remain *finite* and are set by the quantum noise level at $T = 0$ K. Consequently, signal enhancement and synchronization can be achieved even in this very quantum limit, for a properly tuned signal frequency.

1. Introduction

The concept of stochastic resonance was developed in 1981 to explain the nearly periodic occurences of ice ages in the world climate [1, 2]. It is a paradigm of the counterintuitive role that noise can play in nonlinear systems [3]. Generally, stochastic resonance can occur in a nonlinear bistable system subject to a stochastic (noise) and a weak periodic force (signal) [4,5]. Transitions between the associated metastable states occur at random times and are activated by the noise. The periodic drive, by itself insufficient to cause deterministic transitions, leads to a periodic modulation of the transition rates. By variation of the strength of the noise, it has been shown that at an optimal *nonvanishing* noise level the system switches almost periodically between the two states, at the frequency of the applied signal. As the noise is increased beyond this optimal value, the periodicity of the switching is again suppressed. Consequently, the response of the bistable system to a weak coherent signal in the presence of noise undergoes a resonant-like behaviour as the noise level is increased. This phenomenon is called stochastic resonance.

At first sight it might seem surprising that a definite nonvanishing noise level is needed to achieve the most regular response of the system. Nevertheless, the basic mechanism behind this effect is easy to understand: imagine, e.g., the noise level is very low. Then there are very few transitions between the metastable states per modulation period and it is rather unlikely for the stochastic and the periodic driving to act cooperatively, so as to induce periodic transitions. On the other hand, if the noise level is very high, there will be too many transitions during one modulation period, without any correlation between the applied signal and the response of the system. In between, at some intermediate noise level, when the noise-induced transition frequency is near the frequency of the modulation, an optimal synchronization is expected: then it will be most probable that the system jumps from one state to the other and back again exactly once during a modulation cycle. The jumps occur at times when, due to the periodic modulation of the transition rates caused by the applied signal, the ensuing transition rates

0305-4470/99/152895+25$19.50

assume their maxima. Through this cooperativity between the stochastic and the periodic force a periodic signal can be amplified in the presence of noise rather than attenuated [1–22].

The above picture is purely classical: surmounting the threshold which separates the metastable states of the bistable system can only be achieved through the classical stochastic force [23, 24] or its combination with the periodic signal [5]. In the microscopic realm, however, and at sufficiently low temperatures, generic quantum effects such as tunnelling or vacuum fluctuations might alter the picture and provide alternative and efficient transition mechanisms. Indeed, it is quantum tunnelling which renders certain quantum states of molecules metastable [25] and it is the coupling to the electromagnetic vacuum which causes resonance fluorescence of single atoms [26].

As a matter of fact, first studies of two-state systems which undergo quantum tunnelling have shown that stochastic resonance disappears for symmetric transition rates between both states (corresponding to a symmetric tunnelling barrier), in the limit of low temperatures [27–30]. This is essentially due to the relatively weak temperature dependence of the tunnelling rates [31–34] as compared with the exponential sensitivity of the (classical) Kramers rate which resides at the very heart of stochastic resonance in the classical domain [4]. Nonetheless, stochastic resonance can be recovered if one allows for an asymmetry in the threshold seen by the two metastable states, which actually restitutes the desired exponential sensitivity of the transition rates on the temperature [27–30]. Since, here, quantum tunnelling is at the origin of the nonvanishing transition rates between both states, the predicted signal enhancement at finite temperature would be a clear signature of quantum stochastic resonance.

Another contribution [35] has recently demonstrated stochastic resonance in the response of an open, driven quantum system, the micromaser [36–57], to a weak periodic signal. Here, transitions between metastable states of the quantized radiation field coupled to a sequence of two-level atoms are activated by quantum noise induced by the quantum mechanical measurement process on the one hand and by the zero-point fluctuations of the environment on the other. Quantum stochastic resonance allows for the optimal synchronization of quantum jumps between the metastable states of the quantized radiation field with the applied signal at finite temperature [35]. This paper provides a detailed theoretical analysis of this system, illustrated by numerical simulations. In particular, we characterize stochastic resonance displayed by the maser via the signal-to-noise ratio (SNR) on output, as well as via the residence time distribution in either of the metastable states, and study the dependence of signal enhancement and synchronization on the signal frequency on input.

The paper is organized as follows. In the next section, we summarize the basics of micromaser dynamics, with special emphasis on its bistable operation mode [36]. We describe the numerical simulation of a single realization of the maser dynamics, in close analogy to published experimental results, and discuss the origin of the observed quantum jumps between the metastable maser states. Explicit expressions for the relevant transition rates are derived, and the temperature dependence of the latter is analysed. In section 3, we describe quantum stochastic resonance in the micromaser, starting out from an exact numerical solution of the maser master equation under external driving. A properly defined two-state model is shown to reproduce the exact solution very well, provided the intra-well dynamics is *not* completely neglected. Both analytical models are compared with the results of numerical simulations of the maser dynamics. Section 4 concludes the paper.

2. Essentials on the micromaser

Let us start with a short description of the essential features of the quantum system under study. The micromaser, a single mode of the quantized radiation field interacting with a sequence of

two-level atoms and coupled to a dissipative environment, is considered as the experimental realization of 'the protoype of an open, driven quantum system' [37]. It has provided rich experimental evidence for various basic quantum phenomena such as sub-Poissonian photon statistics [54, 55], quantum collapse and revival [52], vacuum Rabi oscillations [51], decoherence of a quantum state [53], Schrödinger cats [53], Heisenberg dogs [57] and quantum jumps [36].

The micromaser [38–40, 42] consists of a single mode resonator which is crossed by a beam of atoms at such a low flux that at most one atom is present in the cavity at the same time. The atoms are initially prepared by a pump laser in a high-lying Rydberg level $|u\rangle$. They enter the cavity in this level, which is resonantly coupled by the cavity mode of frequency ω to a lower-lying Rydberg state $|d\rangle$. The atoms (obtained from a thermal atomic beam) are velocity selected, such that they enter the cavity at a fixed velocity, and consequently interact with the radiation field inside the cavity for a precisely defined interaction time $t_{\rm int}$ (the experimental error of $t_{\rm int}$ is estimated to approximately 1–3% [41]). Hence, they accumulate a well-defined Rabi angle $\phi = \Omega t_{\rm int}$ during the coherent interaction, with Ω the vacuum Rabi frequency, and perform the familiar Rabi oscillations between the upper and the lower states $|u\rangle$ and $|d\rangle$. After exit from the cavity the atoms are detected via ionization in two static electric field regions, which allows one to discriminate between atoms leaving the cavity in $|u\rangle$ or $|d\rangle$. The experimental detection efficiency is essentially limited by the finite spontaneous lifetime $\tau_{\rm se}$ of atomic Rydberg states in free space (after exit from the cavity).

Since all atoms enter the cavity in $|u\rangle$, an atom which is detected in $|d\rangle$ after exit has deposed a photon in the cavity mode during the coherent interaction. Hence, the atoms feed energy into the cavity mode or induce population transfer between the energy eigenstates (the number states $|n\rangle, n \geqslant 0$) of the quantum harmonic oscillator represented by the quantized radiation field. After exit of an atom from the cavity the population of the field evolves like a damped harmonic oscillator, the damping being caused by the coupling of the field mode to the cavity walls which are assumed to be in thermal equilibrium at temperature T. However, the damping rate γ of the cavity is sufficiently small such that before the cavity field has time to relax into the thermal state, the next atom enters the resonator.

The temporal separation of the atoms on entrance to the resonator being Poisson-distributed, with an average given by the inverse of the atomic flux r, the various timescales are arranged such that

$$t_{\rm int} \ll \frac{1}{r} \ll \frac{1}{\gamma}.$$

Consequently, for any initial population distribution $\boldsymbol{p}^{(0)} = (p_0^{(0)}, p_1^{(0)}, p_2^{(0)}, \ldots)$ of the number states of the cavity field (in short: of the 'photon distribution') the maser field will evolve into a stationary state $\boldsymbol{p}^{(\rm ss)}$ [38] which is defined by a dynamical equilibrium where photon losses due to damping will be counterbalanced by the photon gain due to the pumping of the cavity field by the atoms. The actual appearence of this stationary state depends on the various parameters which define the atom–field interaction and the subsequent relaxation. As a matter of fact, $\boldsymbol{p}^{(\rm ss)}$ essentially depends on the so-called pump-parameter $\theta = \phi\sqrt{N_{\rm ex}}$ and on the average thermal photon number $n_b = (\exp(\hbar\omega/kT) - 1)^{-1}$, where $N_{\rm ex} = r/\gamma$ is the atomic flux measured in units of the thermal damping rate. Depending on the choice of θ and n_b, p_n plotted versus n may display one or several maxima, each of them being rather narrow with respect to a Poissonian distribution (this is the origin of sub-Poissonian photon statistics [54, 55] for a single peaked photon distribution).

Throughout this paper, we shall concentrate on the case of a double-peaked distribution of the p_n, which corresponds to the bistable operation mode of the micromaser [36, 39].

Furthermore, we shall neglect the finite spontaneous lifetime τ_{se} and hence the finite detection efficiency in the experiment, as well as the (narrow) velocity spread of the atoms and the consequent error bar of the experimental interaction time of the atoms with the field. All these additional noise sources, which are unavoidable in a real experiment, may shorten the typical timescales of the phenomena we shall report on, without qualitatively changing the effect we are interested in [35]. We expect quantum stochastic resonance in the micromaser to be a robust phenomenon as most nonlinear stabilization phenomena typically are.

2.1. Master equation and stationary state

We now turn to the quantitative description of the maser dynamics and first summarize the relevant results of standard maser theory [37–40, 42].

The photon field in the cavity is described by its density operator. Its evolution equation is well known [39,40], and so is the temporal evolution of populations and coherences. However, for the sake of simplicity, we only deal with states that are diagonal in the photon number representation throughout this paper, choosing the thermal equilibrium state as the initial state of the cavity field. This state is diagonal in the photon number, and due to the maser dynamics any diagonal state remains diagonal for all times. Hence, we can restrict ourselves to the master equation for the diagonal elements of the field density matrix, i.e. for the population of the eigenstates of the harmonic oscillator represented by the cavity field. The time evolution of the ensemble average of the photon field (on timescales longer than $t_{\rm int}$) reads [39]:

$$\dot{p}_n = r[\beta_{n-1}p_{n-1} - \beta_n p_n] + \gamma[n_b n p_{n-1} - (n_b(n+1) + (n_b+1)n)\,p_n + (n_b+1)(n+1)\,p_{n+1}]$$
$$n = 0, 1, 2, \ldots \tag{1}$$

where $\beta_n = \sin^2(\phi\sqrt{n+1})$ describes the probability of detecting an atom in $|d\rangle$ after interaction with n photons in the cavity. The terms proportional to r in (1) describe the coherent interaction between the atoms and the cavity field, the ones proportional to γ, the cavity damping according to the standard master equation for a damped harmonic oscillator. Obviously, a slow (with respect to $t_{\rm int}$) modulation of the atomic flux r can easily be incorporated in our treatment (see section 3 below).

For $t \to \infty$ each solution of (1) will loose the memory of the (normalized) initial condition and approach the following, uniquely determined steady state [38]:

$$p_n^{(\rm ss)} = p_0^{(\rm ss)} \left(\frac{n_b}{n_b+1}\right)^n \prod_{k=1}^{n}\left(1 + \frac{N_{\rm ex}\beta_{k-1}}{n_b k}\right) \qquad n = 1, 2, \ldots \tag{2}$$

which, as already mentioned above, can display one or several maxima as a function of n. $p_0^{(\rm ss)}$ can be obtained from the normalization condition $\sum_{n=0}^{\infty} p_n^{(\rm ss)} = 1$. For sufficiently large values of $N_{\rm ex}$ and finite n_b, (2) can be formally reduced to a form which is parametrized by θ and n_b alone.

In all our subsequent calculations, we use parameter values which we lend from the Garching experiment [36,40–42]: $\gamma = 1/0.06\,{\rm s}^{-1}$, $\Omega = 36\,000\,{\rm rad\,s}^{-1}$, $t_{int} = 28.69 \times 10^{-6}$ s (i.e. $\phi = 1.033$) and $\omega = 2\pi \times 21.506$ GHz. With the choice $N_{\rm ex} = 40$ this gives a pump parameter $\theta = 6.533$, where $\boldsymbol{p}^{(\rm ss)}$ displays two maxima, i.e. the maser operates in the bistable mode. The position of the maxima of $\boldsymbol{p}^{(\rm ss)}$ is independent of the temperature, but not their relative strength, as is obvious from figure 1. Whereas the probability distribution is strongly asymmetric for $T = 0$ K and $T = 2.0$ K, it is close to a symmetric partition between the two maxima localized around photon numbers $n_1 = 6$ and $n_2 = 26$ for $T = 0.6$ K. In addition, for higher temperatures, the maxima are not as distinct as for lower ones and it is more likely to find photon numbers somewhere between the most probable values n_1 and n_2 (notably $\boldsymbol{p}^{(\rm ss)}(n_3 = 13)$ does not vanish any more on the linear scale on the left of figure 1).

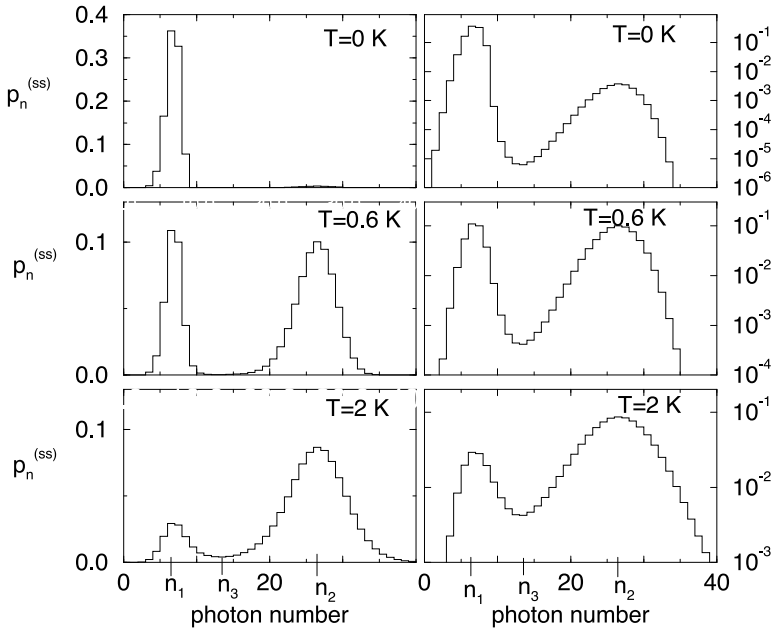

Figure 1. The steady state of the photon distribution for $\theta = 6.533$, $N_{\rm ex} = 40$ and (from top to bottom) $T = 0$ K, 0.6 K, 2.0 K, on a linear (left) and a logarithmic (right) scale, respectively. The positions of the maxima at $n_1 = 6$ and $n_2 = 26$, and of the minimum at $n_3 = 13$ are independent of the temperature, but not their relative strength. For higher temperatures it is more likely to find population at n_3. Up to $T \simeq 2$ K, the minimum $p_{n_3}^{(\rm ss)}$ is still small compared with the maxima $p_{n_1}^{(\rm ss)}$ and $p_{n_2}^{(\rm ss)}$.

Since figure 1 depicts the steady state (2) of the master equation (1), we have to remember that the latter only describes the time evolution of the *ensemble average* of the photon distribution. This implies an average over all random influences on the system. The latter are:

- The noise caused by the measurement of the exiting atoms. A single state reduction destroys the entanglement between the atom and the cavity field mediated by the coherent interaction and allows solely for values 0 or 1 of β read from the detection device. Only averaging over many atoms reproduces the quantum mechanical prediction $0 \leqslant \beta = \sum_n \beta_n p_n \leqslant 1$ [39, 48, 49].
- The noise caused by the interaction with the cavity walls, which has a nonvanishing value even at temperature $T = 0$ K, due to the zero-point fluctuations of the environment. The latter 'stimulate' [26] spontaneous losses from the maser field even at vanishing temperature of the environment.
- The noise introduced by the random (Poisson-distributed) arrival times of the atoms on entrance into the cavity. This amounts to a fluctuation in the damping time of the cavity field between the coherent interactions with two successive atoms [38].

Note that the first two of the above list are sources of *quantum* rather than classical noise. Due to the presence of these noise terms, in a *single realization* of the micromaser, i.e. during the process of subsequent detections of atoms emerging from the resonantor, the photon distribution will actually jump between different number states of the field [39, 48, 49] for most of the time residing in the vicinity of either one of the photon numbers n_1 and n_2 which

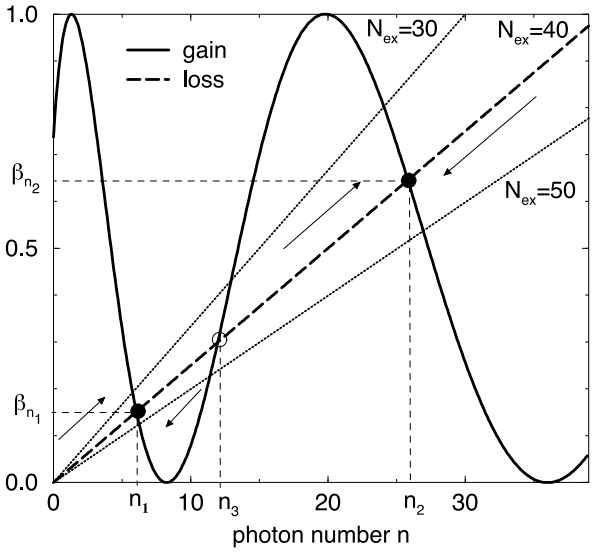

Figure 2. The average gain and loss rate of the photon number. Solid curve: probability β_n for detection of the exiting atoms in $|d\rangle$ versus n, for a Rabi angle $\phi = 1.033$. Since each atom leaving the cavity in $|d\rangle$ adds one photon to the cavity, β_n is the average gain rate of the photon number (in units of the atomic flux r), given n photons in the cavity. Dashed line: average loss rate of the photon number due to damping, for $N_{\rm ex} = 40$ ($\langle \dot{n} \rangle_{loss} = -\gamma n = -r/N_{\rm ex} n$, for $n_b \ll n$, (1)). If the gain rate is higher than the loss rate, n will tend to higher values, and vice versa (as indicated by the arrows). Therefore, of the three points $n_1 \simeq 6$, $n_2 \simeq 26$ and $n_3 \simeq 13$ satisfying the condition 'gain rate equals loss rate', only n_1 and n_2 are stable, corresponding to detection probabilities $\beta_{n_1} \simeq 0.15$ and $\beta_{n_2} \simeq 0.65$. The dotted lines indicate changes of n_1, n_2 and n_3 with $N_{\rm ex}$.

label the maxima of the stationary state in figure 1. A single random event such as the emission of a photon by an atom into the cavity mode enforced by the detection of $|d\rangle$, or the emission or absorption of a photon by the environment, causes a single transition between neighbouring states $n \to n \pm 1$ on a short timescale. The combined action of several such random events causes 'macroscopic' jumps of the maser field between photon states with $n \simeq n_1$ and $n \simeq n_2$, as we shall see in the next paragraph. Since these macroscopic jumps are activated by quantum noise, they provide an experimentally accessible example of quantum jumps between metastable states of a basic quantum system.

2.2. Quantum jumps

Indeed, such quantum jumps have already been observed in the laboratory [36]. Since the direct probing of the resonator field is not possible (any detection device would spoil the quality of the cavity, i.e. enhance its damping rate), the statistical properties of the atom detection ('click statistics') on exit from the cavity are used to infer on the photon statistics inside the cavity [37, 41]. The probabilities of detecting an exiting atom in $|d\rangle$ differ depending on whether the photon distribution is peaked near n_1 or n_2, namely approximately $\beta_{n_1} = n_1/N_{\rm ex}$ or $\beta_{n_1} = n_2/N_{\rm ex}$ (see figure 2). These probabilities can be measured simply by counting the $|d\rangle$-detections during a time interval Δt. Δt must be short compared with the timescale of the jumps but long enough that many ($\gtrsim$100) atoms are detected during Δt (typically, $\Delta t \simeq 0.1$ s). Then, jumps of the detection probability between β_{n_1} and β_{n_2} are a signature of jumps of the cavity field between its metastable states.

Very much like the experiment, a single realization of the micromaser dynamics can be obtained by numerical simulation [39]. By drawing random numbers, the Poisson-distributed arrival times of the atoms are determined. After interaction with the cavity field the *probability* of detecting the atom in $|d\rangle$ is $\beta = \sum_n p_n \beta_n$, where p_n denotes the photon number distribution just before the interaction (i.e. in the moment the atom enters the cavity). In which state the atom is *actually* detected depends on β being larger or smaller than another random number. Subsequent to each detection, the usual quantum mechanical state reduction occurs. For the photon distribution of the cavity field, this implies a 'reset' of the probability distribution [39],

$$p_n{}' = \begin{cases} \dfrac{\beta_{n-1}}{\beta}\, p_{n-1} & n = 1, 2, \ldots, \quad p_0' = 0 \quad \text{detection in } |d\rangle \\ \dfrac{1-\beta_n}{1-\beta}\, p_n & n = 0, 1, 2, \ldots \quad \text{detection in } |u\rangle \end{cases} \tag{3}$$

where p_n' denotes the photon number distribution after the state detection. Between two atoms, the photon field is damped according to the standard master equation for a damped harmonic oscillator (the terms proportional to γ in (1)) [39]. In this way, the numerical simulation of the micromaser defines a stochastic process which is completely characterized by the arrival times of the atoms and the states they are detected in. From this, the corresonding time evolution of the photon number distribution $\boldsymbol{p}(t)$ can be obtained via (3) and the damping master equation.

In order to obtain the characteristic timescales which determine the quantum jumps we need a further refinement of this stochastic process. Indeed, in the above, pumping and damping of the cavity field are not treated on an equal footing. Whereas the pumping is described on the microscopic level of single detection events of individual atoms via (3), the damping step is accounted for by the adequate master equation, which implies an ensemble average. Therefore, at a given time, we still have to deal with a photon *distribution* over the entire photon basis. However, the damping of the field can also be described on a microscopic level, e.g. as the interaction with a second beam of two-level atoms which are weakly coupled to the cavity mode and have an initial state distribution determined by the Boltzmann factor [40]. This additional, weak coupling represents the interaction with the environment through the cavity walls and yields, after a suitable ensemble average, the damping master equation. It allows one to mimic the cavity damping by a sequence of single atom detections of the atoms of the weakly interacting beam, and hence to identify the complete maser dynamics with a jump process on the discrete ladder of number states $|n\rangle$, starting out from a well-defined initial state $|n_0\rangle$. Any such jump is caused by the detection of either a strongly coupled atom after coherent interaction (3), or of a weakly coupled atom during the damping stage. The transition probabilities between adjacent number states per unit time can now be readily read from (1):

$$t_n^+ = \gamma[N_{\rm ex}\beta_n + n_b\,(n+1)] \qquad n \to n+1 \tag{4a}$$

$$t_n^- = \gamma(n_b + 1)\, n \qquad n \to n-1 \tag{4b}$$

with $r = \gamma N_{\rm ex}$. In this picture, which is best adapted for our purpose, the field mode contains a well-defined photon number at any instant of time. It also elucidates the separation of timescales between jumps in the vicinity of either n_1 or n_2, and jumps from the vicinity of n_1 to the vicinity of n_2, respectively. The latter are the manifestation of the bistability of the cavity field: imagine, e.g., there are n photons in the cavity with n close to n_1. The photon number can jump from n to $n-1$ because the cavity walls absorb a photon, or to $n+1$ either because the cavity walls emit a photon, or because an atom is detected in $|d\rangle$. As illustrated in figure 2, the probability of detection in $|d\rangle$ decreases for increasing n around n_1, and therefore the photon number will stay close to n_1 for a long time. Consequently, the photon number n_1 represents a metastable state of the maser. Only as a result of an accidental fluctuation

(figure 2 depicts the average behaviour!) corresponding to a bunching of jumps that *increase* the photon number by one, eventually the photon number can cross the unstable point at n_3, to approach higher values of n. In the region $n > n_3$ the average gain rate of the photon field inside the cavity is higher than the average loss rate and the photon number will quickly approach the second metastable state around n_2. Again, only when, accidentally, a bunching of jumps *decreasing* the photon number by one occurs, can the photon number leave the region around n_2 and approach the metastable state around n_1.

Note that such macroscopic jumps between the vicinity of n_1 and n_2 do also occur at $T = 0$ K. Neither t_n^+ nor t_n^- vanishes in this situation, the timescales only get longer. However, for $n_b = 0$ *solely* the detection of atoms in $|d\rangle$ increases the photon number in the cavity (here we exclude the impact of trapping states $|n_t\rangle$ [50] defined by $\beta_{n_t} = 0$; this can be guaranteed by appropriate choice of $t_{\rm int}$ [39]) and spontaneous losses *alone* decrease the photon number. Hence, the jumps of the maser field between its metastable states are of pure quantum origin. A finite temperature, T, only enhances the thermal fluctuations and reduces the characteristic timescale of the quantum jumps [39].

Finally, figure 2 also illustrates the modulation of the transition rates induced by a modulation of the flux $N_{\rm ex}$. The larger $N_{\rm ex}$, the smaller the separation of the metastable point n_1 and of the unstable point n_3, causing an enhancement of the escape rate from the metastable state labelled by n_1. Simultaneously, increasing $N_{\rm ex}$ increases the separation of n_2 and n_3 and therefore decreases the escape rate from the metastable state associated with n_2. The converse scenario applies for a decrease of $N_{\rm ex}$ and we shall rely on this behaviour in our discussion of stochastic resonance below.

2.3. Transition rates and metastable states

The above description of the maser dynamics as a jump process allows for an explicit calculation of the transition rates between the metastable states of the maser field, in terms of t_n^+ and of the stationary solution $\boldsymbol{p}^{(\rm ss)}$ of (1). Following the general prescription outlined in chapter 7 of [58], the average time for the photon number to switch from n_i to n_f is given by

$$\langle\tau\rangle_{n_i\to n_f} = \sum_{n=n_i}^{n_f} [p_n^{(\rm ss)} t_n^+]^{-1} \sum_{m=0}^{n} p_m^{(\rm ss)} \qquad n_f > n_i \tag{5a}$$

$$\langle\tau\rangle_{n_i\to n_f} = \sum_{n=n_f}^{n_i} [p_n^{(\rm ss)} t_n^+]^{-1} \sum_{m=n}^{\infty} p_m^{(\rm ss)} \qquad n_i > n_f. \tag{5b}$$

Figure 3 shows $\langle\tau\rangle_{n_1\to n}$ and $\langle\tau\rangle_{n_2\to n}$ as a function of n for $\theta = 6.533$, $N_{\rm ex} = 40$, and at temperatures $T = 0.6$ K and $T = 2.0$ K, respectively. n_1 and n_2 again label the metastable maser states. It is evident from the figure that for sufficiently low temperatures the relaxation times in the vicinity of n_1 and n_2 are very short with respect to the timescale for quantum jumps between the metastable states. Under these conditions, the bistable maser operation is very similar to the familiar two-state models which form the basis of most descriptions of stochastic resonance. The transition rates between both metastable states are then given by

$$W_{12} = \langle\tau\rangle_{n_1\to n_2}^{-1} \qquad W_{21} = \langle\tau\rangle_{n_2\to n_1}^{-1} \tag{6}$$

respectively. For large temperatures, the definition of the metastable states is less straightforward as their typical 'lifetimes' become comparable with the intra-state relaxation times (compare the lower panel of figure 3 and figure 1(*c*)), and a two-state model is no more completely adapted to the actual physical situation. We shall come back to this point in section 3.2.

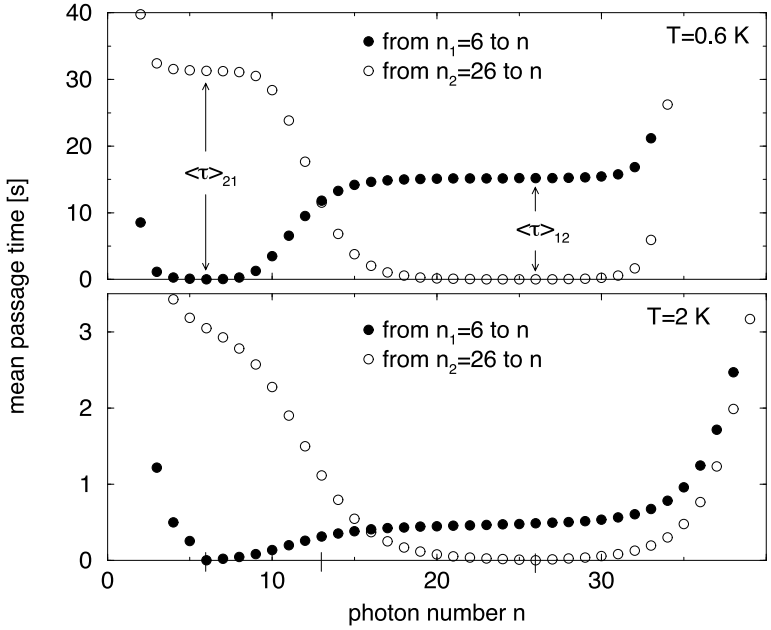

Figure 3. The mean passage time $\langle\tau\rangle_{n_i\to n_f}$ for the photon number to reach the value n, starting from the minima of the steady state distribution $\boldsymbol{p}^{(\mathrm{ss})}$ at $n_1 = 6$ and $n_2 = 26$ (according to (5*a*) and (5*b*)). Top: $T = 0.6$ K, $\theta = 6.533$, $N_{\mathrm{ex}} = 40$. $\langle\tau\rangle_{n_i\to n_f}$ depends only weakly on n_i and n_f, provided n_i is chosen close to n_1 and n_f close to n_2, respectively. In other words, the relaxation times for reaching the local equilibrium distributions around n_1 and n_2 are very small compared with the mean passage times $\langle\tau\rangle_{12}$ and $\langle\tau\rangle_{21}$ from n_1 to n_2. Bottom: $T = 2.0$ K, $\theta = 6.533$, $N_{\mathrm{ex}} = 40$. Local relaxation times and mean passage times $\langle\tau\rangle_{n_1\to n_2}$, $\langle\tau\rangle_{n_2\to n_1}$ become comparable.

Figure 4 shows the transition rates which follow from (6), as a function of $1/T$ and on a logarithmic scale, for two different values of θ and N_{ex}†. In contrast to the familiar Kramers rate for a classical particle in a bistable potential [23, 24], which corresponds to a straight line in such a plot, the maser transition rates saturate for $1/T \to \infty$. This reflects the fact that even at $T = 0$ K transitions are possible, due to the remaining quantum noise sources, see (4*a*) and (4*b*). The saturation sets in earlier for $\langle\tau\rangle_{n_2\to n_1}$, because even at $T = 0$ K the cavity walls can still absorb photons from the mode, thereby enhancing transitions towards smaller photon numbers (see also the upper panel of figure 1). Whereas the choice of $N_{\mathrm{ex}} = 40$ ($\theta = 6.533$) provides symmetric residence times at $T \simeq 0.48$ K, $N_{\mathrm{ex}} = 49.7$ ($\theta = 7.282$) realizes almost symmetric sojourn times in the limit $T = 0$ K. We shall take advantage of this handle on $\langle\tau\rangle_{n_1\to n_2}$ and $\langle\tau\rangle_{n_2\to n_1}$ via N_{ex} (or θ) at the end of section 3.3.

† When comparing figure 4(*a*) with the corresponding results presented in [35], which were obtained from numerical simulations of the micromaser dynamics, a slight deviation will be detected. The reason for this is that in the simulations used in [35], for numerical reasons, the length of the interval between the arrival times of two subsequent atoms (during which the damping of the photon field is performed) was not allowed to exceed a certain upper limit. Therefore, the arrival times of the atoms were not exactly Poisson-distributed, leading to a slightly different effective value of N_{ex}.

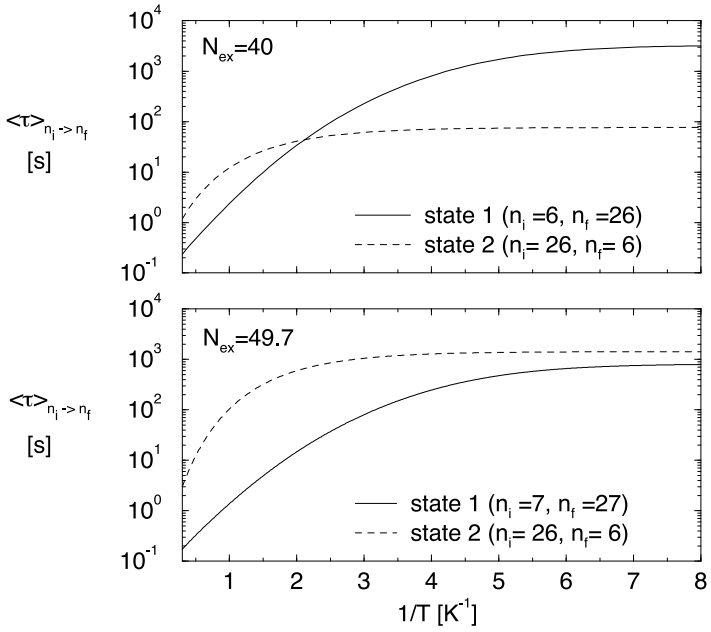

Figure 4. The average residence time $\langle\tau\rangle_{n_1\to n_2}$ in state 1 (centred around the lower photon number $n_1 \simeq 6$), and $\langle\tau\rangle_{n_2\to n_1}$ in state 2 (centred around the higher photon number $n_2 \simeq 26$), versus $1/T$. The curves have been obtained by evaluation of $\langle\tau\rangle_{n_1\to n_2}$ and $\langle\tau\rangle_{n_2\to n_1}$, according to (5*a*) and (5*b*), respectively. A deviation from Kramers' law (a straight line in this semilogarithmic plot) is detected: the rates saturate for $1/T \to \infty$, due to the nonvanishing transition rates between states 1 and 2 at $T = 0$ K, see (4*a*) and (4*b*). These are a consequence of the zero-point fluctuations of the environment and of the coherent coupling of $|u\rangle$ and $|d\rangle$ by the cavity field, respectively, and hence of pure quantum origin. The temperature for which $\langle\tau\rangle_{n_1\to n_2} \simeq \langle\tau\rangle_{n_2\to n_1}$ ('symmetric' transition rates) can be tuned via appropriate choice of θ or $N_{\rm ex}$: (*a*) $\theta = 6.533$, $N_{\rm ex} = 40$. The two curves cross at $T \simeq 0.47$ K, with $\langle\tau\rangle_{n_1\to n_2} = \langle\tau\rangle_{n_2\to n_1} \simeq 44$ s. At $T = 0$ K, $\langle\tau\rangle_{n_1\to n_2} \gg \langle\tau\rangle_{n_2\to n_1}$. (*b*) $\theta = 7.282$, $N_{\rm ex} = 49.7$. $\langle\tau\rangle_{n_1\to n_2} \simeq \langle\tau\rangle_{n_2\to n_1}$ at $T = 0$ K, i.e. symmetric transition rates in the quantum limit $T = 0$ K.

3. Quantum stochastic resonance in the micromaser

We have now set the stage to study the response of the micromaser in its bistable mode to a weak periodic signal which in itself is insufficient to induce periodic switching between the metastable states of the cavity field. Can this quantum device be used to achieve maximum enhancement of the signal, or optimal synchronization with the signal, at a *finite* noise level, much in the spirit of stochastic resonance?

Indeed, it can, as we shall show in the remainder of this paper, where we consider the maser cavity as a sort of nonlinear detection unit. Our input signal is chosen as a modulation of the atomic flux $N_{\rm ex}$, which is also a realistic choice from the experimental point of view. In the laboratory, such a modulation is tantamount to modulating the intensity of the pump laser which prepares the atoms in $|u\rangle$ before they enter the resonator. The output, i.e. the response of our quantum mechanical detection unit to the signal on input is given by the detection probability $\beta(t)$ of the atoms in the lower Rydberg state $|d\rangle$ on exit from the cavity. An enhanced periodicity of the detection signal on output (with the period of the input signal) at finite noise level will then be the signature of stochastic resonance.

To start with, by appropriate choice of signal amplitude $\Delta N_{\rm ex}$ and frequency $\omega_{\rm mod}$, we

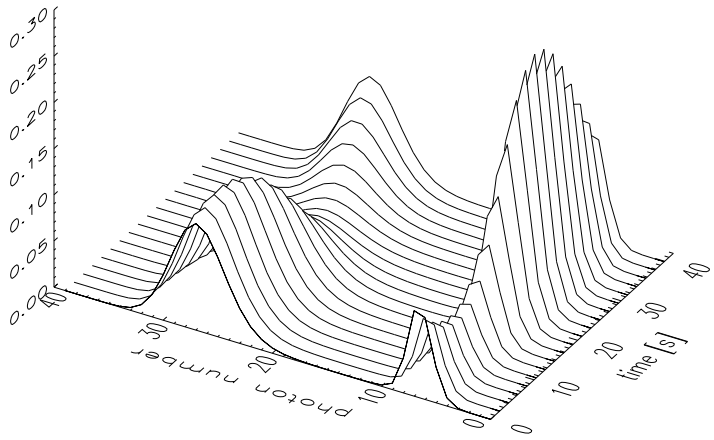

Figure 5. The periodic solution $\boldsymbol{p}^{(\mathrm{ss})}(t)$ of (1). $T = 0.6$ K, $t_{\mathrm{mod}} = 42$ s, $\phi = 1.033$ and $N_{\mathrm{ex}}(t) = 40 + 6.9\cos(2\pi\ t/t_{\mathrm{mod}})$. The bistability of the maser field is preserved over the whole range of N_{ex}.

have to modulate the transition frequencies between the metastable states of the maser field such that:

- the bistability of the dynamics is conserved over an entire modulation period, i.e. ΔN_{ex} must not be too large;
- the modulation period $t_{\mathrm{mod}} = 2\pi/\omega_{\mathrm{mod}}$ roughly matches the timescale of the noise-induced transitions in the absence of driving.

Whereas the choice of ΔN_{ex} can be guided by inspection of figure 2, ω_{mod} can be inferred from figure 4. For the former, we chose $\Delta N_{\mathrm{ex}} = 6.9$, and for the latter we guess that some value of t_{mod} between 10 and 1000 s should do.

Because of the periodicity introduced by the time dependence of $N_{\mathrm{ex}}(t) = \langle N_{\mathrm{ex}}\rangle + \Delta N_{\mathrm{ex}}\sin(\omega_{\mathrm{mod}}t)$, the master equation (1) no longer has a stationary, but rather a time-dependent, periodic solution $\boldsymbol{p}^{(\mathrm{ss})}(t) = \boldsymbol{p}^{(\mathrm{ss})}(t + t_{\mathrm{mod}})$, which will be approached for any normalized initial condition in the limit $t \to \infty$. Figure 5 shows an example for $T = 0.6$ K, $N_{\mathrm{ex}} = 40$, $\Delta N_{\mathrm{ex}} = 6.9$, $t_{\mathrm{mod}} = 42$ s. As required above, the bistability is conserved over the entire range of N_{ex} (i.e. the modulation is 'small'). Figure 6 shows the corresponding output of the maser, i.e. the temporal evolution of the detection probability $\beta(t)$ on exit, for different values of the temperature of the environment. This result was obtained by the simulation procedure outlined in section 2.2 above. The figure shows that the best synchronization of the quantum jumps is achieved for $T \simeq 0.6$ K (see also the figures 8–10 and 17 below). However, a visual inspection alone of plots like the ones in figure 6 is generally insufficient to judge the achieved signal enhancement (as a consequence of the generally large background noise). We therefore need a quantitative measure of stochastic resonance and turn first to the most familiar quantity used in this context, the SNR.

3.1. Signal-to-noise ratio

In terms of the SNR on output, stochastic resonance is defined as a maximum of the SNR at a *finite* value of the strength of the noise on input [4]. In our case, the strength of the input noise is controlled via the temperature T. The SNR is extracted from the power spectrum of $\beta(t)$ as illustrated in figure 7. At the signal frequency $\omega_{\mathrm{mod}} = 2\pi/t_{\mathrm{mod}}$ (as well as at higher

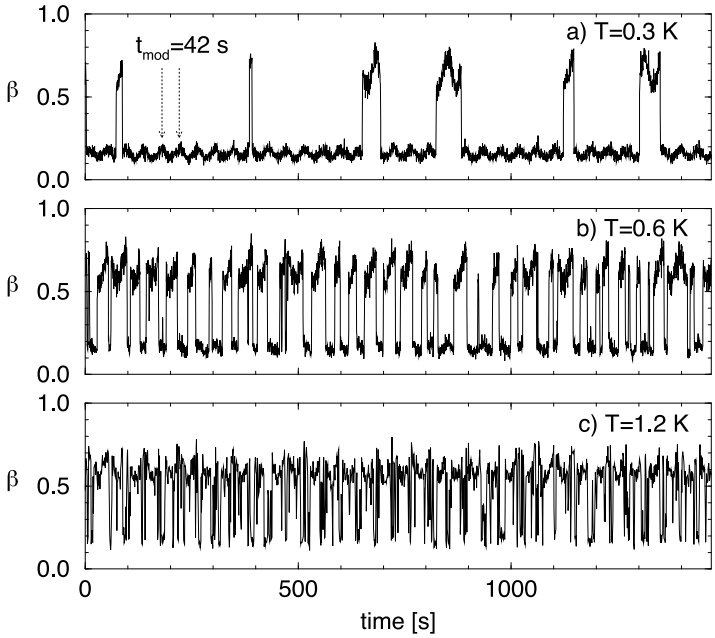

Figure 6. The time evolution of the probability β to detect an atom in $|d\rangle$ with periodically modulated atomic flux $N_{\rm ex}(t) = 40 + 6.9\cos(2\pi\ t/t_{\rm mod})$. β is obtained from the simulation of the maser dynamics (as decribed in section 2.2) by counting the atomic detections during time intervals of length $\Delta t = 0.5$ s. $t_{\rm mod} = 42$ s, $\phi = 1.033$ and (*a*) $T = 0.3$ K, (*b*) 0.6 K, (*c*) 1.2 K. The noise-induced synchronization of quantum jumps is poor for the lowest temperature (rare quantum jumps), optimal for the intermediate temperature (almost regular quantum jumps) and again poor for the highest temperature (too frequent quantum jumps).

harmonics), there is a sharp peak (the signal peak), the rest of the spectrum (the noise part) has approximately Lorentzian shape. The SNR is given by the area under the signal peak, after subtraction of the noise background, divided by the amplitude of the noise spectrum at the signal frequency†.

The power spectrum of $\beta(t)$ can either be directly obtained from the simulation of the maser dynamics, i.e. by a Fourier transform of the detection signal of figure 6 (much as an experimentalist would do), or it can be calculated *exactly* as follows. The autocorrelation function of $\beta(t)$ reads

$$C(\tau) = \langle\langle \beta(t+\tau)\ \beta(t)\rangle\rangle_{t_{\rm mod}}$$

where we average over the signal period and over the ensemble of jump processes which we introduced in the motivation of (4*a*) and (4*b*). The ensemble average can be performed by summation over all possible photon numbers m at time t and n at time $t+\tau$, where the

† Note that there is a difference between the theoretical definition of the SNR and the—pragmatic—definition typically used in experiments [4]. The experimental definition compares the total output power (i.e. the sum of output noise and signal) with the background noise level, at the signal frequency. Consequently, the experimental SNR is a dimensionless quantity which never decreases below unity. Since increasing the available integration time makes the signal peak sharper and higher, the experimental SNR increases with the experimental sampling time. In contrast, the theoretical SNR, defined as the ratio of the *area* under the signal peak and of the background noise power at the signal frequency, has the dimension of frequency and is independent of the integration time.

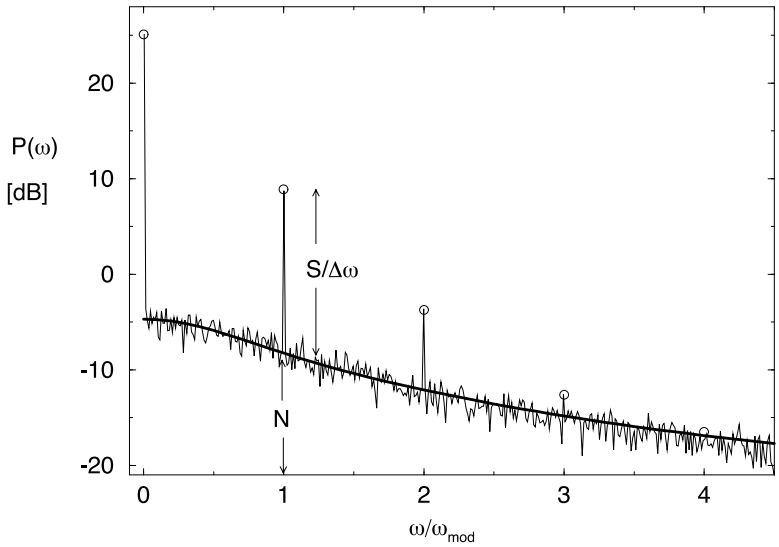

Figure 7. Power spectral density of the detection signal $\beta(t)$ on output from the maser cavity, for $T = 0.6$ K, $t_{\rm mod} = 42$ s, $\langle N_{\rm ex}\rangle = 40$, $\Delta N_{\rm ex} = 6.9$. Thin curve: result of a simulation of the maser dynamics (see section 2.2 and figure 6 above), averaged over 20 runs of 2.5 million atoms each. Thick curve and circles: predictions of (9) and (8), respectively.

corresponding statistical weights $p_m(t)$ and $p_n(t+\tau)$ obey the master equation (1). Therefore,

$$C(\tau) = \sum_{m,n=0}^{\infty} \beta_n \beta_m \langle p_n(t+\tau|m,t)\, p_m^{(\rm ss)}(t)\rangle_{t_{\rm mod}}. \tag{7}$$

Here, $p_n(t+\tau|m,t)$ is the probability of finding n photons in the cavity mode at time $t+\tau$, given m photons at time t. $p_m^{(\rm ss)}(t)$ specifies the probability to find m photons at time t, with no knowledge about previous times $t' < t$. As we know, $p_n(t+\tau|m,t)$ approaches the periodic solution $p_n^{(\rm ss)}(t+\tau)$ of (1) for $\tau \to \infty$. Therefore, in the limit $\tau \to \infty$, $C(\tau)$ approaches a periodic function $C^{\rm S}(\tau)$ given by

$$C^{\rm S}(\tau) = \sum_{m,n=0}^{\infty} \beta_n \beta_m \langle p_n^{(\rm ss)}(t+\tau)\, p_m^{(\rm ss)}(t)\rangle_{t_{\rm mod}} \qquad C^{\rm S}(\tau) = C^{\rm S}(\tau + t_{\rm mod}).$$

By virtue of the Wiener–Khinchine theorem [59], the power spectrum of $\beta(t)$ is the Fourier transform of the autocorrelation function $C(\tau)$. From the above $C^{\rm S}(\tau)$ we get δ-peaks at $\omega = 0$, $\omega = \omega_{\rm mod}$, and at higher harmonics of the signal frequency. The output signal power S is then defined [4] as the coefficient in front of the δ-function at $\omega = \omega_{\rm mod}$ (corresponding to the area under the signal peak)

$$S = \frac{2\pi}{t_{\rm mod}} \int_0^{t_{\rm mod}} {\rm d}\tau\ \cos(\omega_{\rm mod}\tau) C^{\rm S}(\tau) \tag{8}$$

whereas the output noise power N is the height of the noise spectrum at $\omega_{\rm mod}$:

$$N = 2\int_0^{\infty} {\rm d}\tau\ \cos(\omega_{\rm mod}\tau)(C(\tau) - C^{\rm S}(\tau)). \tag{9}$$

The exact temperature dependence of S, N and the SNR in the maser output is illustrated in figures 8–10†. They show the results of the evaluation of (8) and (9), for different modulation

† S, N and SNR are measured in dB in figures 8–10, with S[dB] $= \log_{10} S$. Since N has the dimension of time, N [dB] and SNR [dB] are defined up to an additive constant given by the employed unit of time.

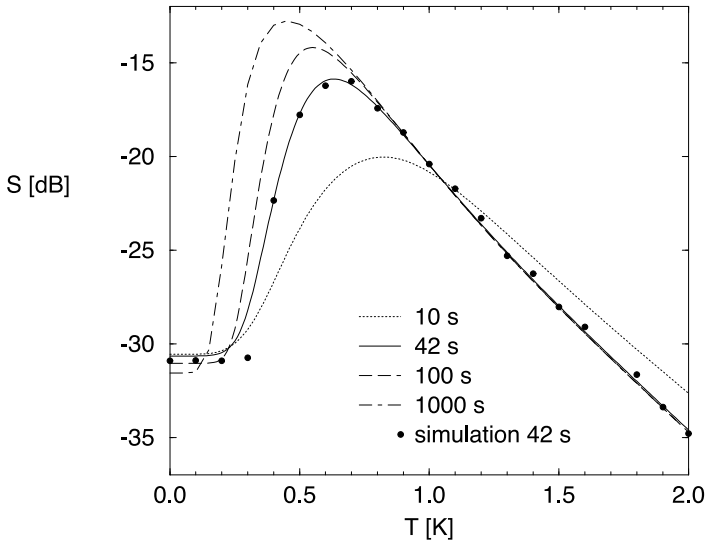

Figure 8. The signal output S for $\langle N_{\rm ex}\rangle = 40$, $\Delta N_{\rm ex} = 6.9$, $\phi = 1.033$ and different modulation periods $t_{\rm mod}$. The signal exhibits its maximum at $T = 0.82$ K ($t_{\rm mod} = 10$ s), $T = 0.63$ K ($t_{\rm mod} = 42$ s), $T = 0.55$ K ($t_{\rm mod} = 100$ s) and $T = 0.23$ K ($t_{\rm mod} = 1000$ s), respectively. The circles show the results of the simulation of the maser dynamics, for comparison (for each value of T the simulation was run for 50 million atoms).

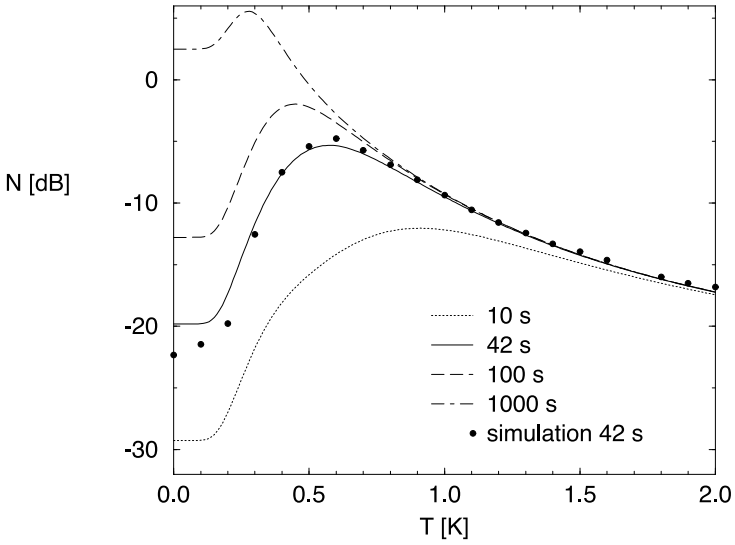

Figure 9. The noise output N for $\langle N_{\rm ex}\rangle = 40$, $\Delta N_{\rm ex} = 6.9$, $\phi = 1.033$ and different modulation periods $t_{\rm mod}$. The noise exhibits its maximum at $T = 0.87$ K (for $t_{\rm mod} = 10$ s), $T = 0.57$ K (for $t_{\rm mod} = 42$ s), $T = 0.45$ K (for $t_{\rm mod} = 100$ s) and $T = 0.27$ K (for $t_{\rm mod} = 1000$ s), respectively.

periods $t_{\rm mod} = 10$ s, 42 s, 100 s and 1000 s. The value $t_{\rm mod} = 42$ s was chosen since for this period, at $T = 0.55$ K, $\langle N_{\rm ex}\rangle = 40$, $\Delta N_{\rm ex} = 6.9$ and $\phi = 1.033$, the average residence times in both metastable states are equal to $\frac{1}{2}t_{\rm mod} = 21$ s, defining a 'symmetric' situation (because the modulation of $N_{\rm ex}$ slightly changes the transition rates, the average residence times in the two

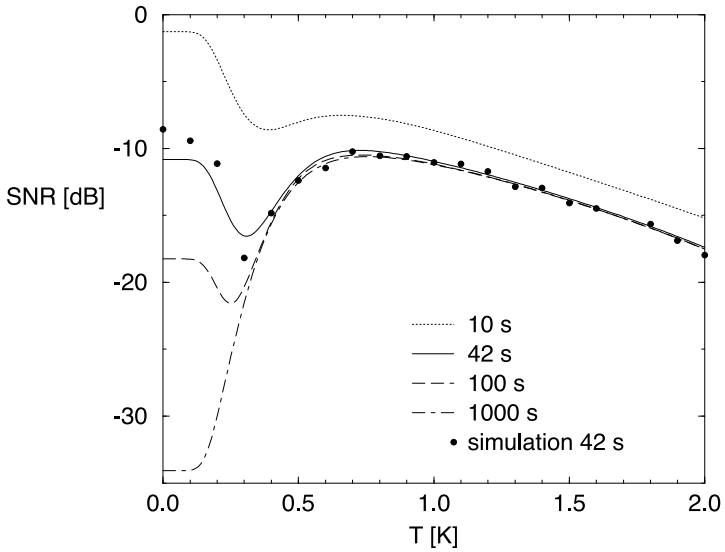

Figure 10. The SNR on output, for $\langle N_{ex}\rangle = 40$, $\Delta N_{ex} = 6.9$, $\phi = 1.033$ and different modulation periods. The local maximum of the SNR at temperatures $T \leqslant 0.2$ K (for $t_{mod} \leqslant 100$ s) is due to dominant intra-state dynamics at such low temperatures. As soon as the increasing temperature induces appreciable jumps between the metastable states (i.e. on a timescale no longer negligible compared with the modulation period t_{mod}), the SNR increases up to $T \simeq 0.7$ K (in all cases), where it exhibits a maximum, a signature of stochastic resonance.

states intersect at a slightly different temperature than in the unmodulated case of figure 4). The maxima of the output signal power S (figure 8) occur at $T = 0.82$ K ($t_{mod} = 10$ s), $T = 0.63$ K ($t_{mod} = 42$ s), $T = 0.55$ K ($t_{mod} = 100$ s) and $T = 0.45$ K ($t_{mod} = 1000$ s). For comparison, equality between t_{mod} and the sum of the modulation free (i.e. $N_{ex}(t) = \langle N_{ex}\rangle$) average residence times in the two metastable states is realized for $T = 1.12$ K ($t_{mod} = 10$ s), $T = 0.63$ K ($t_{mod} = 42$ s), $T = 0.47$ K ($t_{mod} = 100$ s) and $T = 0.24$ K ($t_{mod} = 1000$ s). For modulated N_{ex} one finds $T = 1.01$ K ($t_{mod} = 10$ s), $T = 0.55$ K ($t_{mod} = 42$ s), $T = 0.43$ K ($t_{mod} = 100$ s) and $T = 0.23$ K ($t_{mod} = 1000$ s), respectively. Hence, the original matching condition formulated for the choice of t_{mod} as compared with the *unmodulated* average residence times [1] is excellent in the case of symmetric rates ($t_{mod} = 42$ s and $T = 0.63$ K), and slightly worse for the asymmetric case. The discrepancy in the asymmetric case just underlines the approximate nature of the matching condition.

The maxima of the output noise power N (figure 9) are attained at slightly different temperatures from those for maximum signal power: $T = 0.87$ K ($t_{mod} = 10$ s), $T = 0.57$ K ($t_{mod} = 42$ s), $T = 0.45$ K ($t_{mod} = 100$ s) and $T = 0.27$ K ($t_{mod} = 1000$ s). However, as for the signal power, the 'optimal' temperature decreases as the modulation period increases, in agreement with the temperature dependence of the transition rates displayed in figure 4.

Finally, combining the graphs for S and N yields the SNR in figure 10: at low temperatures, the maser output is largely governed by intra-state dynamics (cf figure 6(*a*)). Provided the noise level is sufficiently low for low T (this is the case for $t_{mod} \leqslant 100$ s in figure 9) this suggests a signal enhancement at very low temperatures in figure 10, which, however, does *not* reflect macroscopic jumps of the maser field between its metastable states. Due to the slightly nonsimultaneous temperature dependence of S and N, the SNR then first decreases over a finite interval of T, until the temperature is large enough to induce appreciable transitions at

the signal frequency. This causes an increase of the SNR up to temperatures around $T \simeq 0.7$ K, where a maximum is observed for *all* modulation periods. Hence, the maser displays quantum stochastic resonance on output. The largest enhancement factor of approximately 25 dB is achieved for a modulation period $t_{\mathrm{mod}} \simeq 1000$ s, which is of the order of the sum of the average residence times in the quantum limit of figure 4, at very low temperatures $T < 0.25$ K $(1/T > 4)$. We checked that the enhancement factor cannot be improved by choosing even slower modulation periods $t_{\mathrm{mod}} = 3000$–$10\,000$ s. For $T \leqslant 0.2$ K, S, N and SNR are nearly constant because of the saturation of the transition rates for $T \to 0$ K.

Let us finally stress that figures 8–10 also show S, N and SNR for $t_{\mathrm{mod}} = 42$ s as obtained from the simulation of the micromaser dynamics (described in section 2.2). The results agree very well with those obtained from (8) and (9), which underlines the consistency of our results.

3.2. Two-state model

In the preceding calculation of the SNR, we made use of the master equation (1), which describes the complete dynamics of the photon distribution, without making explicit use of the existence of a bistability. In order to get a better intuitive understanding, however, it is instructive to focus our attention on the jumps between the metastable states of the cavity field. Therefore, we come back to the picture developed in section 2.3, and assume that at any time the maser field can only be in either one of the two bistable states. The equations (5*a*), (5*b*) and (6), which specify the interstate transition rates W_{12} and W_{21} keep their validity for time-dependent N_{ex}, provided N_{ex} is modulated adiabatically, i.e. for modulation periods t_{mod} much longer than the relaxation time for reaching intra-state equilibrium (a condition which is fulfilled for all the modulation periods we consider; compare the long and the short timescales in figure 3). This provides us with periodically modulated transition rates $W_{12}(t)$ and $W_{21}(t)$, as illustrated in figure 11.

Given the transition rates $W_{12}(t)$ and $W_{21}(t)$, the power spectrum of $\beta(t)$ in the two-state model can be calculated in much the same way as demonstrated above for the exact calculation. We denote by m_1 the probability of the system residing in the metastable state centred around n_1 (in short: 'state 1' hereafter). $m_2 = 1 - m_1$ is then the probability for photon numbers close to the centre n_2 of the second metastable state (in short: 'state 2'; also see figure 1). For the ensemble-averaged time evolution of m_1, the following rate equation applies [27]:

$$\dot{m}_1 = -W_{12}(t)m_1 + W_{21}(t)(1 - m_1). \tag{10}$$

Similar to the master equation (1), (10) also has a periodic solution $m_1^{(\mathrm{ss})}(t)$, which will be approached by any solution of (10) for $t \to \infty$ (see (2.2) of [27] for an analytical expression for $m_1^{(\mathrm{ss})}(t)$). Now we can calculate the autocorrelation function of the detection probability $\beta(t)$, which in the two-state model switches between two values $\beta^{(1)}$ and $\beta^{(2)}$, corresponding to state 1 and 2. Approximately, $\beta^{(1)} = \beta_{n_1}$ and $\beta^{(2)} = \beta_{n_2}$, where n_1 and n_2 are the positions of the maxima of the steady state distribution $\boldsymbol{p}^{(\mathrm{ss})}$ for $N_{\mathrm{ex}} = \langle N_{\mathrm{ex}} \rangle$ (see figure 1). The autocorrelation function $\tilde{C}$ for the two-state model consequently reads:

$$\tilde{C}(\tau) = \sum_{i,j=1}^{2} \beta^{(i)}\beta^{(j)} \langle m_i(t+\tau\,|\,j,t) m_j^{(\mathrm{ss})}(t) \rangle_{t_{\mathrm{mod}}}. \tag{11}$$

In analogy to the foregoing paragraph, $m_i(t+\tau\,|\,j,t)$ is the probability of occupying state i at time $t+\tau$, provided the maser was in state j at time t. $m_j^{(\mathrm{ss})}(t)$ gives the probability to occupy state j at time t, without knowledge of the previous history. As we know, $m_i(t+\tau\,|\,j,t)$ approaches the periodic solution $m_i^{(\mathrm{ss})}(t+\tau)$ of (10) for $\tau \to \infty$. Therefore, $\tilde{C}(\tau)$ approaches a periodic function for $\tau \to \infty$, and output signal power S and noise power N can be determined in the same way as in section 3.1.

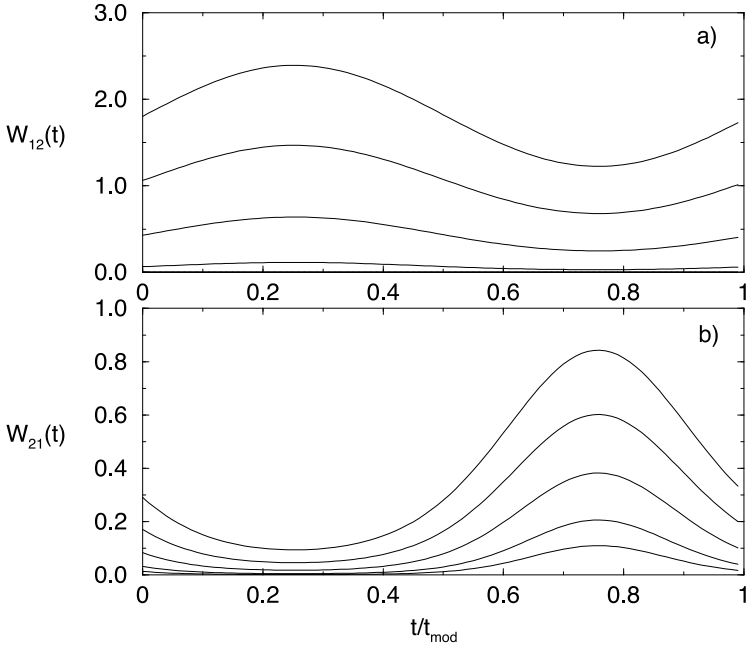

Figure 11. The periodic modulation of the transition rates from (*a*) state 1 ($n_1 \simeq 6$) to 2 ($n_2 \simeq 26$) and (*b*) state 2 to 1, for (from bottom to top) $T = 0.2$ K, 0.6 K, 1.0 K, 1.4 K and 1.8 K. $\phi = 1.033$, $N_{\rm ex}(t) = 40 + 6.9\sin(2\pi\ t/t_{\rm mod})$. In (*a*), the curve for $T = 0.2$ K cannot be distinguished from the t-axis. As expected, the average of W_{12} and W_{21} over one modulation period increases with increasing T. As a particular property of the micromaser, also the modulation amplitude of W_{12} and W_{21} increases with increasing T.

Figures 12–14 show the corresponding results for S, N and SNR in the two-state model. The signal exhibits a maximum at about the same temperature as the exact solution, but it decreases more slowly at large T and no maximum in the SNR can be observed. The reason for this discrepancy is that by introducing two *constant* detection probabilities $\beta^{(1)}$ and $\beta^{(2)}$, we neglected the intra-state dynamics, i.e. the modulations of $\beta^{(1)}$ and $\beta^{(2)}$ caused by the dynamics of the photon distribution in the vicinity of n_1 and n_2, respectively. Since the relaxation time for reaching intra-state equilibrium is very small (see figure 3), there is practically no contribution from the intra-state dynamics to the noise (see figure 13). However, there *is* a contribution to the signal because the local equilibrium distributions around n_1 and n_2 depend on $N_{\rm ex}$, and are therefore also periodically modulated (this is easily observed in figure 6(*a*)). This leads to periodically modulated probabilities $\beta^{(1)}(t)$ and $\beta^{(2)}(t)$ for the detection of an atom in $|d\rangle$, during the time the maser field resides in the corresponding metastable state 1 or 2, respectively. A good approximation for $\beta^{(1,2)}(t)$ can actually be obtained by determining the intersection points of the gain and loss rate for each value of $N_{\rm ex}(t)$ in figure 2. Doing so and replacing $\beta^{(1,2)}$ by $\beta^{(1,2)}(t)$ in (11), we obtain the results for the 'improved two-state model', characterized by periodically modulated transition rates $W_{12}(t)$ and $W_{21}(t)$ between periodically modulated detection probabilities $\beta^{(1)}(t)$ and $\beta^{(2)}(t)$.

Figures 12–14 show that these results agree with the exact ones ((8) and (9)) very well up to $T \simeq 2$ K. We remember (see section 2.1 and figure 3) that at higher temperatures, a two-state model cannot be expected to give exact results because then the bistability of the maser field is not as pronounced as at low temperatures (see figure 1). This is manifest in

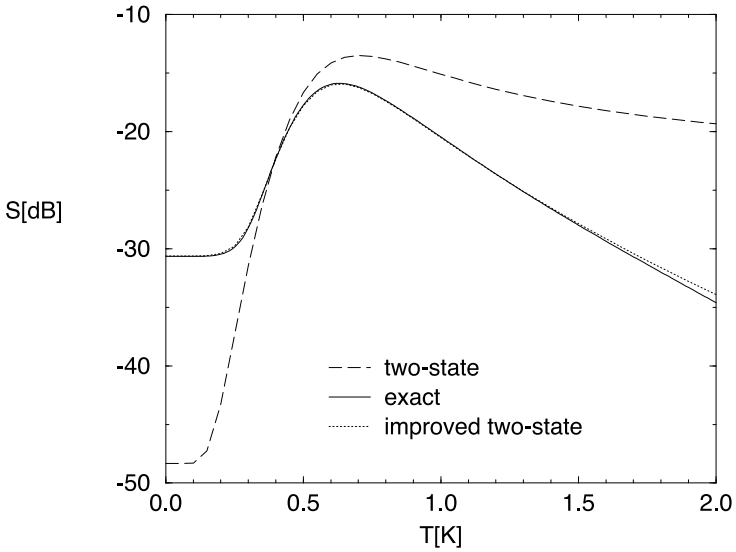

Figure 12. The signal output S for the two-state model and the improved two-state model, compared with the result of the exact solution (8). $\langle N_{\rm ex}\rangle = 40$, $\Delta N_{\rm ex} = 6.9$, $\phi = 1.033$ and $t_{\rm mod} = 42$ s. The improved two-state model agrees with the exact results very well. At low temperatures, the signal is mainly caused by the intra-state dynamics. At high temperatures, the intra-state dynamics weaken the output signal power S.

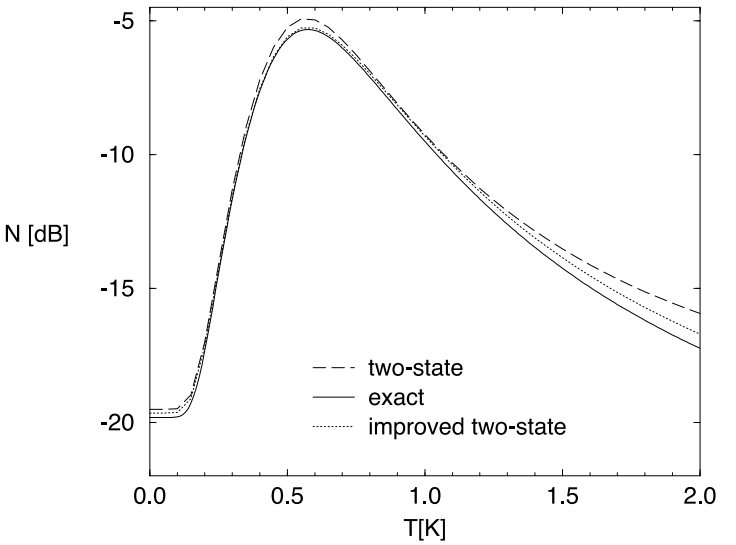

Figure 13. Noise output N for the two-state model and the improved two-state model, compared with the result of the exact solution (9). $\langle N_{\rm ex}\rangle = 40$, $\Delta N_{\rm ex} = 6.9$, $\phi = 1.033$ and $t_{\rm mod} = 42$ s. N is rather insensitive to the intra-state dynamics, since the relaxation time for reaching intra-state equilibrium is small compared with the modulation period $t_{\rm mod}$.

the observation that at higher temperatures the intra-state relaxation time is no longer small compared with the residence times in either of the two states (see the lower panel of figure 3).

Note that the improved two-state model improves comparison with the exact result in the

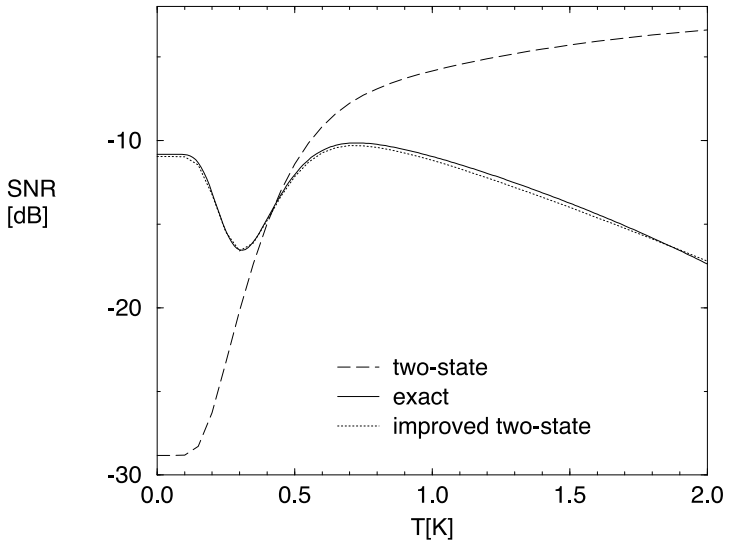

Figure 14. The SNR on output for the two-state model and the improved two-state model, compared with the exact result of (8), (9). $\langle N_{\rm ex}\rangle = 40$, $\Delta N_{\rm ex} = 6.9$, $\phi = 1.033$ and $t_{\rm mod} = 42$ s. The improved two-state model agrees very well with the exact results. In the simple two-state model no maximum in the SNR is observed, since the ouput signal power S decreases less rapidly with increasing T (see figure 12).

low-temperature *as well as* in the high-temperature regime. For temperatures below $T \simeq 0.3$ K this is obvious because of the periodic intra-state modulation which can be observed, e.g. in figure 6(*a*). The cause for the improvement is less obvious for temperatures above $T \simeq 0.5$ K. A first hint is given by examination of the periodic modulation of the transition rates shown in figure 11. Not only does the average of the rates over one modulation cycle increase with T, but also the *amplitude* of the rate modulation, in contrast to the standard scenario of stochastic resonance. Consequently, in the simple two-state model the signal power will decrease rather slowly with increasing T, and hence the SNR does not decrease at all. Taking into account the periodic modulation of $\beta^{(1)}(t)$ and $\beta^{(2)}(t)$ allows us to compensate for this effect. For sufficiently high temperatures, during one modulation cycle a large number of noise-induced jumps between the metastable states will occur, and the ratio of the probabilities m_1 and m_2 for the system to reside in state 1 and 2 is essentially given by

$$\frac{m_1(t)}{m_2(t)} = \frac{W_{21}(t)}{W_{12}(t)}.$$

On the other hand, $\beta^{(1)}(t)$ and $\beta^{(2)}(t)$ are modulated such that they are *maximal* when $W_{21}(t)$ takes it *maximum* value (compare the figures 11(*b*) and 2), i.e. when the system most likely resides in state 1 (the detection probability is then $\beta(t) = \beta^{(1)}(t) < \beta^{(2)}(t)$, see figure 2). For the same reason, $\beta^{(1)}(t)$ and $\beta^{(2)}(t)$ take their *minimum* values at the *maxima* of $W_{12}(t)$, i.e. when the maser field resides most likely in state 2, with a detection probability $\beta(t) = \beta^{(2)}(t) > \beta^{(1)}(t)$ (see figure 2). Consequently, the periodic modulation of $\beta^{(1)}(t)$ and $\beta^{(2)}(t)$ around β_{n_1} and β_{n_2} *decreases* the contrast of the detection signal $\beta(t)$ as compared with the difference between the fixed values $\beta^{(1)} = \beta_{n_1}$ and $\beta^{(2)} = \beta_{n_2}$. This induces a faster decrease of the signal with increasing T as compared with the simple two-state model, and explains the success of the improved two-state model apparent from the figures 12–14.

3.3. Residence-time distributions

We have seen above that the response of the micromaser to a weak periodic signal indeed displays a maximum in the SNR on output, a characteristic feature of stochastic resonance. In this final paragraph, we now want to quantify this phenomenon in a somewhat complementary way, by the residence-time distribution $V(\tau)$ [5, 12, 27, 28] of the maser field in either of its metastable states 1 and 2, centred around photon numbers n_1 and n_2, respectively (see figure 1).

Whereas the SNR characterizes stochastic resonance in terms of spectral amplification, $V(\tau)$ essentially probes synchronization of the system reponse with the input signal. If there is no periodic forcing, the transition rates between the two metastable states are constant, and consequently $V(\tau)$ decays exponentially, with a decay constant given by the average residence time in either of the metastable states. When adding a signal, i.e. a periodic modulation of the transition rates (see section 3.2 and figure 11), there appears equally spaced maxima on top of the exponential of $V(\tau)$. These peaks are easy to understand: let us assume that at time t_1 the transition rate $W_{12}(t)$ has a maximum and the system jumps from state 1 to state 2. Now the system resides in state 2 for a time τ and then jumps back again to state 1 at time $t_2 = t_1 + \tau$. This will be more likely if at time t_2 the corresponding transition rate $W_{21}(t)$ also takes its maximum value. If the transition rates are modulated in phase opposition as in our case, see figure 11 (i.e. $W_{21}(t)$ assumes its maximum half a modulation period later than $W_{12}(t)$), this will be the case at $\tau^{(k)} = (2k+1)t_{\mathrm{mod}}/2$, $k = 0, 1, 2, \ldots$. Hence, $V(\tau)$ will exhibit maxima at times $\tau^{(k)}$. Note that $V(\tau)$ is, by definition, *independent* of the intra-state dynamics of either one of the metastable states, and, consequently, there is no difference between the simple and the improved two-state model introduced in the preceding section.

Figure 15 shows an example of $V(\tau)$ deduced from (10), compared with the result obtained from a numerical simulation of the maser dynamics (see section 2.2). Starting from the time-dependent transition rates (6) obtained from the two-state model (with periodically modulated N_{ex}), we calculated $V(\tau)$ exactly following the prescription given in section III of [27]. The physical situation represented in the figure is the same as the one shown in figure 6(*b*) or in figures 8–10, for $t_{\mathrm{mod}} = 42$ s and $T = 0.6$ K. Clearly, the residence time distributions in state 1, $V^{(1)}(\tau)$, as well as in state 2, $V^{(2)}(\tau)$, deviate from an exponential decay to be expected in the absence of a periodic drive. Whereas $V^{(1)}(\tau)$ exhibits a shoulder before being essentially damped out above $\tau \simeq t_{\mathrm{mod}}$ by the exponential envelope, $V^{(2)}(\tau)$ displays a maximum rather precisely at $\tau^{(0)}$, an indication of the synchronization with the input signal through stochastic resonance, and also appears to indicate a second maximum at $\tau^{(1)}$. Furthermore, both $V^{(1)}(\tau)$ and $V^{(2)}(\tau)$ are peaked at $\tau = 0$, a signature of noise-induced, uncorrelated transitions between the metastable maser states.

To allow some comparison with the above results for the SNR, we still need the temperature dependence of $V(\tau)$. This is illustrated in figure 16, compared with an exponential distribution $V^{(\mathrm{exp})}(\tau)$ (with the same average residence time at the given temperature, $V^{(\mathrm{exp})}(\tau) = \exp(-\tau/\tau_{\mathrm{av}})/\tau_{\mathrm{av}}$, where $\tau_{\mathrm{av}} = \int_0^\infty \mathrm{d}\tau\, \tau V(\tau)$). In state 1, at low temperatures, long residence times are probable and the distribution exhibits many peaks, thus reducing the strength of the first peak. At high temperatures, short residence times are probable and the distribution decays practically to zero before $\tau = \frac{1}{2}t_{\mathrm{mod}}$ is reached. Therefore, at some intermediate temperature (between 0.5 K and 0.6 K) the strength of the first peak exhibits a maximum. The residence times in state 2 do not depend as strongly on the temperature T as in state 1 (because the saturation of the transition rates sets in earlier for state 2, see figure 4, and, hence, the temperature dependence of $V(\tau)$ is less pronounced in the limit of small T). However, it can clearly be seen that the first maximum of $V(\tau)$ gets smaller for higher temperatures, $T > 0.6$ K.

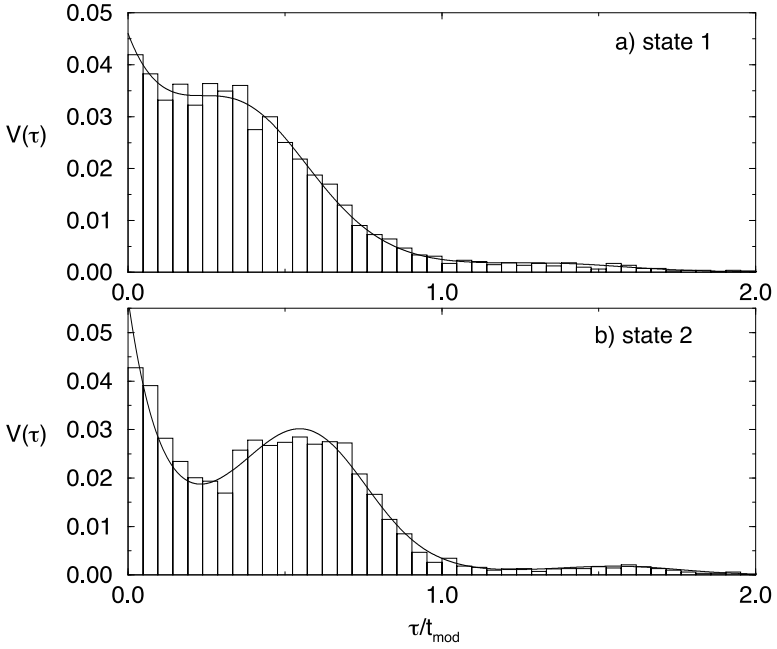

Figure 15. The distribution of residence times in (*a*) state 1 (with the lower photon number $n_1 \simeq 6$) and (*b*) state 2 (with the higher photon number $n_2 \simeq 26$). $T = 0.6$ K, $t_{\mathrm{mod}} = 42$ s, $\langle N_{\mathrm{ex}} \rangle = 40$, $\Delta N_{\mathrm{ex}} = 6.9$, $\phi = 1.033$. The results from the simulation (histograms) agree perfectly well with the prediction of the simple two-state model (solid curve).

To make these considerations more precise, it is necessary to quantify the strength of the first maximum of $V(\tau)$ at $\tau^{(0)}$. In [5], it was proposed to simply consider the area under the peak, $P_1 = \int_{(\frac{1}{2}-\alpha)t_{\mathrm{mod}}}^{(\frac{1}{2}+\alpha)t_{\mathrm{mod}}} V(\tau)\,\mathrm{d}\tau$, with $0 < \alpha \leqslant \frac{1}{4}$ (the actual value of α is immaterial for the behaviour of P_1). As a function of the temperature, it was shown that $P_1(T)$ goes through a maximum. However, $P_1(T)$ also exhibits a maximum in the absence of any modulation on input (i.e. for exponential $V(\tau)$) [5], since the above definition essentially sets a matching condition with respect to a preselected average residence time $\tau = \frac{1}{2}t_{\mathrm{mod}}$. Therefore, we alternatively suggest to consider the difference between $V(\tau)$ and the corresponding exponential distribution $V^{(\mathrm{exp})}(\tau)$, and introduce the following measure for the strength S_1 of the first peak,

$$S_1 = \int_{\tau_1}^{\tau_2} \mathrm{d}t\,(V(\tau) - V^{(\mathrm{exp})}(\tau)).$$

Here, τ_1 and τ_2 are defined by $V(\tau_{1,2}) = V^{(\mathrm{exp})}(\tau_{1,2})$, $\tau_1 < \frac{1}{2}t_{\mathrm{mod}}$, $\tau_2 > \frac{1}{2}t_{\mathrm{mod}}$ and $V(\tau) > V^{(\mathrm{exp})}(\tau)$ for $\tau_1 < \tau < \tau_2$. In contrast to P_1, S_1 only measures the synchronization due to the modulation of the transition rates rather than the mere matching of timescales. Since it is the modulaton of the transition rates that makes for the occurence of stochastic resonance, a maximum in $S_1(T)$ as a function of the temperature can be considered as an unambiguous signature of stochastic resonance. Figure 17 shows the dependence of S_1 on T, for the parameters of the figures 8–10 (cf also figure 16). For the slower modulation periods $t_{\mathrm{mod}} \leqslant 100$ s, S_1 exhibits a maximum in state 1 and fairly large values in state 2. Stochastic resonance is most pronounced here for the intermediate modulation periods $t_{\mathrm{mod}} = 42$ s (maximum of S_1 at $T = 0.56$ K) and $t_{\mathrm{mod}} = 100$ s (maximum of S_1 at $T = 0.46$ K), at temperatures where the residence times in state 1 and state 2 are roughly equal (see section 3.1).

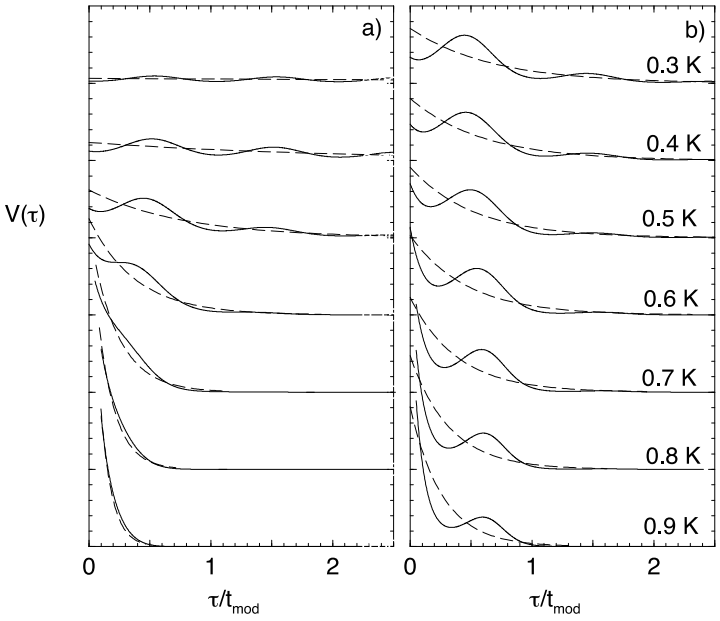

Figure 16. Distribution of residence times (a) in state 1 (with the lower photon number $n_1 \simeq 6$) and (b) in state 2 (with the higher photon number $n_2 \simeq 26$) for $T = 0.3$–0.9 K. $\langle N_{\rm ex}\rangle = 40$, $\Delta N_{\rm ex} = 6.9$, $\phi = 1.033$ and $t_{\rm mod} = 42$ s. In this temperature range, the residence times in state 2 are less sensitive to changes in T, due to the earlier saturation of the transition rates from state 2 to 1. Dashed curves: exponential distribution with the same average as the corresponding solid curve.

The cases of $t_{\rm mod} = 10$ s (maximum at $T = 0.8$ K) and $t_{\rm mod} = 1000$ s (maximum at $T = 0.27$ K) are less favourable, and S_1 vanishes in state 2 for the longest modulation period, since even for low temperatures the residence times in this state are much shorter than $\frac{1}{2}t_{\rm mod}$.

For all values of $t_{\rm mod}$, the 'optimal' temperature is not too far from the temperatures which yield optimal signal enhancement in the figures 8 and 10. However, the comparison of the figures 8–10 and 17 for $t_{\rm mod} = 1000$ s clearly shows that optimal signal enhancement is not necessarily equivalent to optimal synchronization. Since the average residence times are very asymmetric at low temperatures for $\langle N_{\rm ex}\rangle = 40$, as illustrated by figure 4(a), the low-frequency driving with $t_{\rm mod} = 1000$ s cannot induce optimal synchronization despite a signal enhancement of 25 dB in the SNR. However, as illustrated in figure 4(b), a slight change in $\langle N_{\rm ex}\rangle$ allows for almost symmetric residence times in the quantum limit $T = 0$ K, and figure 18 shows that for $\langle N_{\rm ex}\rangle = 49.7$ K (with all other parameters of figure 17 unchanged) optimal synchronization of the quantum jumps of the maser field with the applied signal is achieved by tuning the signal to the residual transition rates at $T = 0$ K, corresponding to a modulation period $t_{\rm mod} = 1590$ s.

4. Conclusion

In this paper, we have shown that a fundamental *and experimentally realized* quantum system, the micromaser, exhibits stochastic resonance on output when driven by a weak periodic signal on input. The effect is most pronounced (with a signal enhancement of approximately 25 dB) for driving periods which match the sum of the residual quantum transition rates between the

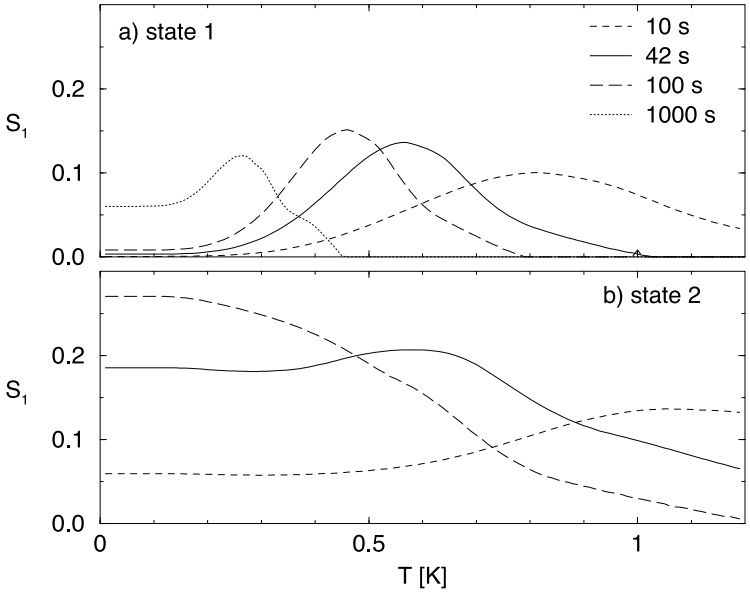

Figure 17. The strength S_1 of the first peak in the residence-time distribution $V(\tau)$ in (*a*) state 1 (with the lower photon number $n_1 \simeq 6$) and (*b*) state 2 (with the higher photon number $n_2 \simeq 26$), for different modulation periods $t_{\rm mod}$. $\langle N_{\rm ex}\rangle = 40$, $\Delta N_{\rm ex} = 6.9$, and $\phi = 1.033$. S_1 exhibits a maximum in state 1 and fairly large values in state 2, with the exception of the largest modulation period $t_{\rm mod} = 1000$ s. In the latter case, the residence times in state 2 are much shorter than $\frac{1}{2}t_{\rm mod}$, even at low temperatures (due to residual quantum noise), and S_1 vanishes.

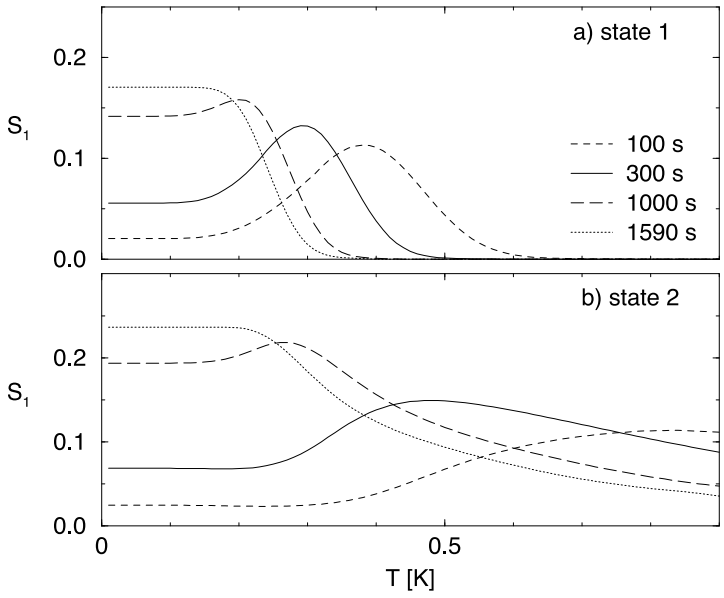

Figure 18. The same as figure 17, but $\langle N_{\rm ex}\rangle = 49.7$. For this average atomic flux, the residence times in state 1 and 2 are closest to each other in the limit $T = 0$ K (see figure 4(*b*)). Consequently, optimal synchronization of the quantum jumps of the maser field with the signal is achieved when the signal period is tuned to the residual transition rates at $T = 0$ K.

metastable states of the maser field at $T = 0$ K, i.e. when the input signal is tuned to the quantum noise level inherent in the maser dynamics. However, an optimal signal enhancement in the SNR does not necessarily correspond to an optimal synchronization of the maser output with the input signal (as quantified by S_1), since the latter requires symmetric residence times in the metastable states of the cavity field. Such a symmetric situation at $T = 0$ K can, nonetheless, be established by the appropriate choice of $\langle N_{\rm ex}\rangle$ (or θ), which is an experimentally well-controlled parameter.

In our treatment, we focused on the basic scenario for stochastic resonance, which can also be directly implemented in state of the art experiments. However, some very intriguing questions have not been discussed here and shall be dealt with in future work. Let us just open up some perspectives:

- In the above, we observed stochastic resonance in the detection probability $\beta(t)$ of an atom in the lower Rydberg state $|d\rangle$, on exit from the cavity. The statistics of the detector clicks completely determine the statistics of the photon distribution inside the cavity and vice versa [37]. However, the SNR of the average photon number in the cavity mode (replace $\beta_n\beta_m$ by nm in (7)) does *not* exhibit a maximum as T increases, but rather increases (with decreasing slope) at large temperatures (up to $T \simeq 3$ K) [60]. Consequently, the maximum in the SNR observed for $\beta(t)$ must be encoded in the higher correlation functions of the photon distribution. This provides an explicit example highlighting the importance of the appropriate choice of the output variable to observe stochastic resonance in the SNR [12], and will be discussed in more detail in a separate contribution.
- This work starts out with incoherent pumping of the maser field, i.e. there are no correlations induced between different number states of the cavity field. The latter can be generated by feeding the cavity with atoms which are prepared in a coherent superposition of $|u\rangle$ and $|d\rangle$ [44]. The signature of stochastic resonance in the coherences remains hitherto completely unexplored.

Acknowledgments

It is a pleasure to thank Rosario N Mantegna for fruitful exchanges, as well as for constructive comments on our manuscript. We also enjoyed entertaining discussions with Peter Hänggi in Sion.

References

[1] Benzi R, Sutera A and Vulpiani A 1981 *J. Phys. A: Math. Gen.* **14** L453
[2] Benzi R, Parisi G, Sutera A and Vulpiani A 1982 *Tellus* **34** 10
[3] Science and Technology *Come feel the noise* The Economist 1995 July 29th p 61
[4] McNamara B and Wiesenfeld K 1989 *Phys. Rev.* A **39** 4854
[5] Gammaitoni L, Hänggi P, Jung P and Marchesoni F 1998 *Rev. Mod. Phys.* **70** 223
[6] Benzi R, Parisi G, Sutera A and Vulpiani A 1983 *SIAM J. Appl. Math.* **43** 565
[7] Douglass J K, Wilkens L, Pantazelou E and Moss F 1993 *Nature* **365** 337
[8] Fauve S and Heslot F 1983 *Phys. Lett.* A **72** 3506
[9] Rouse R, Han S and Lukens J E 1994 *Appl. Phys. Lett.* **66** 108
[10] Reimann P and Hänggi P 1998 *Chaos* **8** 629
[11] Bartusek R, Hänggi P and Jung P 1994 *Phys. Rev.* E **49** 3930
[12] Eckmann J P and Thomas L E 1982 *J. Phys. A: Math. Gen.* **15** L261
[13] Simon A and Libchaber A 1992 *Phys. Rev. Lett.* **68** 3375
[14] Mantegna R N and Spagnolo B 1994 *Phys. Rev.* E **49** R1792
[15] Castelpoggi F and Wio H S 1997 *Europhys. Lett.* **38** 91
[16] Fox R F and Lu Y 1993 *Phys. Rev.* E **48** 3390

[17] Roy R, Short R, Durnin J and Mandel L 1980 *Phys. Rev. Lett.* **45** 1486
[18] Vemuri G and Roy R 1989 *Phys. Rev.* A **39** 4668
[19] Bulsara A R and Gammaitoni L 1996 *Phys. Today* **March** 39
[20] Ginzburg S L and Pustovoit M A 1998 *Phys. Rev. Lett.* **80** 4840
[21] Stocks N G and Manella R 1998 *Phys. Rev. Lett.* **80** 4835
[22] Jung P and Hänggi P 1989 *Europhys. Lett.* **8** 505
[23] Kramers H 1940 *Physica* **7** 284
[24] Hänggi P, Talkner P and Borkovec M 1990 *Rev. Mod. Phys.* **62** 251
[25] Cohen-Tannoudji C C, Diu B and Laloë F 1973 *Mécanique Quantique* vol I (Paris: Hermann)
[26] Sargent M, Scully M O and Lamb W 1974 *Laser Physics* (London: Addison-Wesley)
[27] Löfstedt R and Coppersmith S 1994 *Phys. Rev.* E **49** 4821
[28] Löfstedt R and Coppersmith S 1994 *Phys. Rev. Lett.* **72** 1947
[29] Grifoni M and Hänggi P 1996 *Phys. Rev. Lett.* **76** 1611
[30] Grifoni M and Hänggi P 1996 *Phys. Rev.* E **54** 1390
[31] Grabert H, Weiss U and Hänggi P 1984 *Phys. Rev. Lett.* **52** 2193
[32] Grabert H and Weiss U 1985 *Phys. Rev. Lett.* **54** 1605
[33] Fisher M and Dorsey D 1985 *Phys. Rev. Lett.* **54** 1609
[34] Grifoni M, Sassetti M, Hänggi P and Weiss U 1995 *Phys. Rev.* E **52** 3596
[35] Buchleitner A and Mantegna R N 1998 *Phys. Rev. Lett.* **80** 3932
[36] Benson O, Raithel G and Walther H 1996 *Phys. Rev. Lett.* **72** 3506
[37] Briegel H J, Englert B G, Sterpi N and Walther H 1994 *Phys. Rev.* A **49** 2962
[38] Filipowicz P, Javanainen J and Meystre P 1986 *Phys. Rev.* A **34** 3077
[39] Haroche S 1991 *Fundamental Systems in Quantum Optics (Les Houches 53)* ed J Dalibard, J M Raimond and J Zinn-Justin (Amsterdam: Elsevier)
[40] Englert B G 1994 *19th Int. Nathiagali Summer College on Physics and Contemporary Needs* ed S A Ahmad and S M Farooqi (India: Pak Book Cooperation) in press
[41] Englert B G *et al* 1998 *Fortschr. Phys.* **46** 897
[42] Raithel G, Wagner C, Walther H, Narducci L M and Scully M O 1994 *Cavity Quantum Electrodynamics* ed P R Berman (Boston, MA: Academic) p 57
[43] Krause J, Scully M O and Walther H 1987 *Phys. Rev.* A **36** 4547
[44] Wagner C, Brecha R J, Schenzle A and Walther H 1993 *Phys. Rev.* A **47** 5068
[45] Englert B G *et al* 1996 *Phys. Rev.* A **53** 4386
[46] Maître X *et al* 1997 *Phys. Rev. Lett.* **79** 769
[47] Meschede D, Walther H and Müller G 1985 *Phys. Rev. Lett.* **54** 551
[48] Meystre P 1987 *Opt. Lett.* **12** 669
[49] Meystre P and Wright E M 1988 *Phys. Rev.* A **37** 2524
[50] Meystre P, Rempe G and Walther H 1988 *Opt. Lett.* **13** 1078
[51] Brune M *et al* 1996 *Phys. Rev. Lett.* **76** 1800
[52] Rempe G, Walther H and Klein N 1987 *Phys. Rev. Lett.* **58** 353
[53] Brune M *et al* 1996 *Phys. Rev. Lett.* **77** 4887
[54] Rempe G, Schmidt-Kaler F and Walther H 1990 *Phys. Rev. Lett.* **64** 2783
[55] Rempe G and Walther H 1990 *Phys. Rev.* A **42** 1650
[56] Brune M *et al* 1987 *Phys. Rev. Lett.* **59** 1899
[57] Bergou J A and Englert B G 1998 *J. Mod. Opt.* **45** 701
[58] Gardiner C W 1983 *Handbook of Stochastic Methods* (Berlin: Springer)
[59] Loudon R 1983 *The Quantum Theory of Light* (Oxford: Oxford University Press)
[60] Wellens T 1998 Stochastische Resonanz im Mikromaser *Diploma Thesis* Ludwig-Maximilians-Universität München